Hindawi Publishing Corporation
Journal of Nanomaterials
Volume 2016, Article ID 4878935, 8 pages
http://dx.doi.org/10.1155/2016/4878935

Research Article

Influence of Reaction Solvent on Crystallinity and Magnetic Properties of $MnFe_2O_4$ Nanoparticles Synthesized by Thermal Decomposition

Lina Song, Changzhi Yan, Wei Zhang, Haoan Wu, Zhengyang Jia, Ming Ma, Jun Xie, Ning Gu, and Yu Zhang

State Key Laboratory of Bioelectronics, Jiangsu Key Laboratory for Biomaterials and Devices, School of Biological Science and Medical Engineering and Collaborative Innovation Center of Suzhou Nano Science and Technology, Southeast University, Nanjing 210096, China

Correspondence should be addressed to Ning Gu; guning@seu.edu.cn and Yu Zhang; zhangyu@seu.edu.cn

Received 12 March 2016; Revised 20 May 2016; Accepted 14 June 2016

Academic Editor: Balachandran Jeyadevan

This study reports the synthesis of three kinds of manganese-doped magnetic ferrite nanoparticles ($MnFe_2O_4$) in benzyl ether, octyl ether, and 1-octadecene by a simple and low cost thermal decomposition method. It was found that benzyl ether results in a dramatic improvement in nanoparticle crystallinity owing to its stronger reducibility compared to octyl ether and 1-octadecene, as demonstrated by X-ray diffraction and TEM measurements. Raman spectroscopy detection also indicated that the reducing solvent of benzyl ether was in favor of forming magnetite-like structure ferrite, while maghemite-like structured ferrite was obtained in octyl ether and 1-octadecene. The saturation magnetization (M_S) of $MnFe_2O_4$ synthesized in benzyl ether was 85 emu/g [Fe], which was 3 and 5 times larger than $MnFe_2O_4$ synthesized in octyl ether and 1-octadecene, respectively. The specific absorption rate (SAR) of $MnFe_2O_4$ nanoparticles synthesized in benzyl ether was 574 W/g, while $MnFe_2O_4$ nanoparticles synthesized in octyl ether and 1-octadecene have had much smaller SAR of 76 and 33 W/g, respectively. $MnFe_2O_4$ nanoparticles synthesized in benzyl ether also exhibit higher relaxivity (r_2 = 207 mM^{-1} s^{-1}) than those synthesized in octyl ether and 1-octadecene (r_2 = 65 and 22 mM^{-1} s^{-1}). It was obvious that $MnFe_2O_4$ nanoparticles synthesized in reducing benzyl ether have higher crystallinity and thus higher M_S, SAR, and r_2 values, which can serve as a better candidate for hyperthermia and magnetic resonance imaging.

1. Introduction

The biomedical applications of magnetic nanoparticles, such as cell marking, magnetic resonance imaging (MRI), drug delivery, and hyperthermia, are strongly dependent on their magnetic properties [1–3]. The development of nanoparticles with superior magnetic properties has drawn much attention [4–7]. Synthetic strategies based on thermal decomposition of iron acetylacetonate ($Fe(acac)_3$) can provide high-quality magnetic nanoparticles [8]. In general, the size of nanoparticles is an important parameter to control their magnetic properties. The magnetic properties of core-shell nanoparticles vary with the core size [9]. In a certain extent, the saturation magnetization (M_S) and relaxation rate (r_2) increased with the core size of magnetic nanoparticles. In addition, the synthetic strategy based on the metal dopant substitution could provide magnetic ferrite nanoparticles with high and tunable magnetic properties. This has been proved by Cheon group, where Mn^{2+}, Co^{2+}, and Ni^{2+} ions doped ferrite nanoparticles were synthesized and $MnFe_2O_4$ nanoparticles exhibited highest M_S values and provided good MRI contrast effect [5, 10]. Compared with cobalt and nickel, manganese can offer better biocompatibility. Actually, mangafodipir trisodium (MnDPDP, Teslascan), a Mn^{2+}-containing complex contrast agent, has been used to enhance hepatic MRI examinations in clinic [11], implying that Mn^{2+}-doped nanoparticles have a potential to develop biomedical applications. In addition, its strong magnetism can also help reduce the administration dosage.

1,2-Hexadecanediol was used to provide a reductive environment for the thermal decomposition of $Fe(acac)_3$ in the classical synthetic strategies developed by Sun group [12]. They had also demonstrated that the presence of excess amount of oleylamine (OAm) can provide a strong reductive environment [13]. In this case, excess amount of OAm was used as not only surfactant but also reducing reagent. Note that different kinds of reaction solvent, such as phenyl ether, benzyl ether, octyl ether, and 1-octadecene, were used in synthesis based on thermal decomposition of $Fe(acac)_3$ [3, 6, 12, 13]. However, there are few studies on the influence of different reaction solvents on the structure and properties of magnetic nanoparticles. Herein, we studied the influence of different kinds of reaction solvents on the magnetic properties of nanoparticles synthesized by thermal decomposition of $Fe(acac)_3$ and $Mn(acac)_2$. Keeping the amount of surfactants (oleylamine and oleic acid) constant, three kinds of Mn^{2+}-doped magnetic nanoparticles ($MnFe_2O_4$) were synthesized in the solvent of benzyl ether, octyl ether, and 1-octadecene, respectively. And the relationship among magnetism, structure, and solvent reducibility was investigated.

2. Experimental

2.1. Materials. Reagents used in the synthesis are all commercially available without further treatment. Iron(III) acetylacetonate ($Fe(acac)_3$, 98%), oleic acid ($C_{17}H_{33}COOH$, 85%), oleylamine ($C_{18}H_{35}NH_2$, 90%), and benzyl ether ($C_7H_7OC_7H_7$, 97%) were purchased from Aladdin Chemical Reagent Co., Ltd. (China). 1-Octadecene ($C_{18}H_{36}$, 90%) and manganese(II) acetylacetonate ($Mn(acac)_2$, 97%) were purchased from Alfa Aesar. Chloroform (99%), hexanes (85%), ethanol (95%), and acetone (99%) were purchased from Sinopharm Chemical Reagent Co., Ltd. (China). Octyl ether ($C_8H_{17}OC_8H_{17}$, 95%) was purchased from J&K Chemical Reagent Co., Ltd. 1,2-Distearoyl-sn-glycero-3-phosphoethanolamine-N-[methoxy(polyethyleneglycol)-2000] (DSPE-PEG2000) was purchased from Avanti Polar Lipids. The deionized water we used was prepared in our laboratory by Aquapro water purification machine (EDI1-1001-U, Yiyang, China).

2.2. Synthesis of $MnFe_2O_4$ Nanoparticles. According to Scheme 1, the synthesis of $MnFe_2O_4$ nanoparticles is made as follows: 1 mmol of $Fe(acac)_3$ and 0.5 mmol $Mn(acac)_2$ were dissolved in 10 mL of solvent (benzyl ether for preparation of $MnFe_2O_4$ nanoparticles of MFO-1, octyl ether for MFO-2, and 1-octadecene for MFO-3) containing 4.5 mmol of oleic acid (OA) and 1.5 mmol of OAm under N_2 atmosphere. The solution was heated up from room temperature to 220°C at a heating rate of 3.3°C/min and kept at this temperature for 60 min. Then the solution was heated up to 290°C at a heating rate of 3.3°C/min. After refluxing for 30 min, the solution was cooled down at room temperature. The reaction product was washed with ethanol and separated by using magnet. The obtained black precipitate of manganese ferrite nanoparticles ($MnFe_2O_4$) could be dispersed in nonpolar organic solvents, such as chloroform and isooctane.

2.3. Synthesis of DSPE-PEG2000 Coated $MnFe_2O_4$ Nanoparticles. The $MnFe_2O_4$ nanoparticles were transferred to aqueous media by encapsulating with DSPE-PEG2000. 6 mg of $MnFe_2O_4$ nanoparticles (MFO-1, MFO-2, and MFO-3) was dissolved in chloroform (5 mL) containing 9 mg of DSPE-PEG2000. The solution was vaporized under vacuum by heating to 65°C for 30 min to completely remove chloroform. Then the samples were dissolved in deionized water (5 mL) followed by sonication for 5 minutes. Excess unreacted micelles and large aggregates were removed by centrifugation. Three kinds of hydrosoluble manganese ferrite nanoparticles (PEG-MFO-1, PEG-MFO-2, and PEG-MFO-3) were obtained.

2.4. Characterization. The morphology, crystal structure, and crystal orientation of MFO-1, MFO-2, and MFO-3 were characterized with a transmission electron microscopy (TEM, JEOL, Tokyo) and X-ray diffraction (XRD, Siemens D-500). The Raman spectra were measured in a wavelength range between 200 and 1000 nm at room temperature (InVia, Renishaw). The magnetic properties were studied with a vibrating sample magnetometer (VSM 7407, Lakeshore) at 300 K. The specific absorption rate (SAR) values of $MnFe_2O_4$ nanoparticles under alternating magnetic field (ACMF) (SPG-06-III, Shuangping) were detected by an optic fiber thermometer (UM18, FISO, Canada). The correlative relaxivity coefficients (r_2) were tested on clinical magnetic resonance imaging scanner (MRI, Avanto 1.5 T, Siemens).

3. Results and Discussion

Monodisperse $MnFe_2O_4$ nanoparticles were synthesized by thermal decomposition in different solvents (benzyl ether for MFO-1, octyl ether for MFO-2, and 1-octadecene for MFO-3). The TEM images and size distribution diagrams of nanoparticles are shown in Figures 1 and 2. The results indicate that MFO-1 is cubic with an average core diameter of 10.1 nm, while MFO-2 and MFO-3 are spherical with core size of 9.8 nm and 10.2 nm, respectively. It is reported that the shape of ferrite nanoparticles can be determined by changing initial molar ratios of OA and OAm [14]. The synthesis of $MnFe_2O_4$ nanoparticles in different solvents was processed in the case of unchanged materials input of OA and OAm. Thus the morphology of them relies on the reaction solvents. As discussed above [12, 13], the reductive environment is important for the thermal decomposition reaction. In general, benzyl ether acts as antioxidant which is turned into benzaldehyde and benzoic acid in the presence of oxygen. As a result, benzyl ether provided a stronger reductive environment than octyl ether and 1-octadecene in the reaction process. The reductive environment facilitated the decomposition of $Fe(acac)_3$ and $Mn(acac)_2$ at a low temperature and promoted the transformation of Fe^{3+} to Fe^{2+}, which is conducive to the formation of $MnFe_2O_4$ nanoparticles [12, 13, 15, 16]. Thus, the monomer formation and nucleation in benzyl ether were much earlier and faster than the other two. In this case, the formed monomer was more rapidly consumed and the formed $MnFe_2O_4$ nanoparticles earlier entered into kinetic control growth process from thermodynamic control

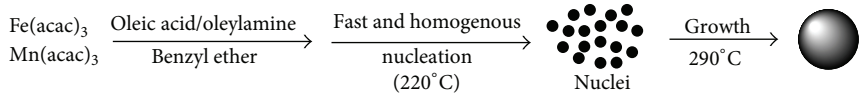

Scheme 1: Schematic synthetic process of $MnFe_2O_4$ nanoparticles.

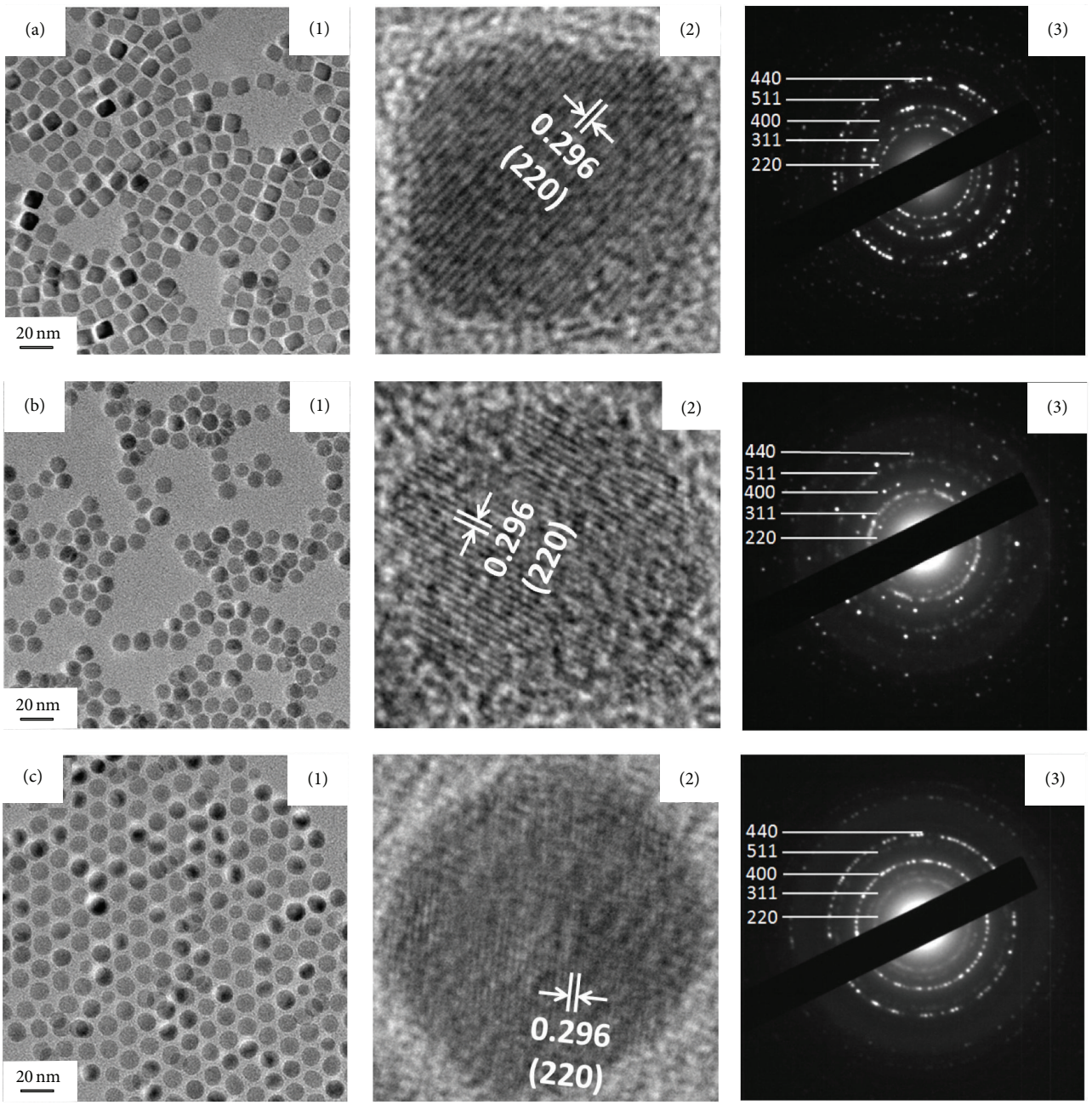

Figure 1: TEM images, HRTEM images, and electron diffraction patterns of $MnFe_2O_4$ nanoparticles MFO-1 (a), MFO-2 (b), and MFO-3 (c).

reaction. The typical spinel structure of ferrite nanocrystal is based on a face-centered cubic (fcc) model with three low-energy facets, {100}, {110}, and {111} [17] (Figure 3(b)). The {111} planes possess the highest surface energy. Hence, the low monomer concentration induced the preferential growth along {111} direction [18], resulting in the formation of cubical nanocrystals (MFO-1) in benzyl ether. In contrast, the thermodynamic control growth was dominant in the synthetic duration of $MnFe_2O_4$ nanoparticles in octyl ether and 1-octadecene, resulting in the formation of spherical nanoparticles.

The measured lattice fringes of these nanoparticles (MFO-1, MFO-2, and MFO-3) are all 0.296 nm, corresponding with the lattice spacing of {220} planes of spinel structure

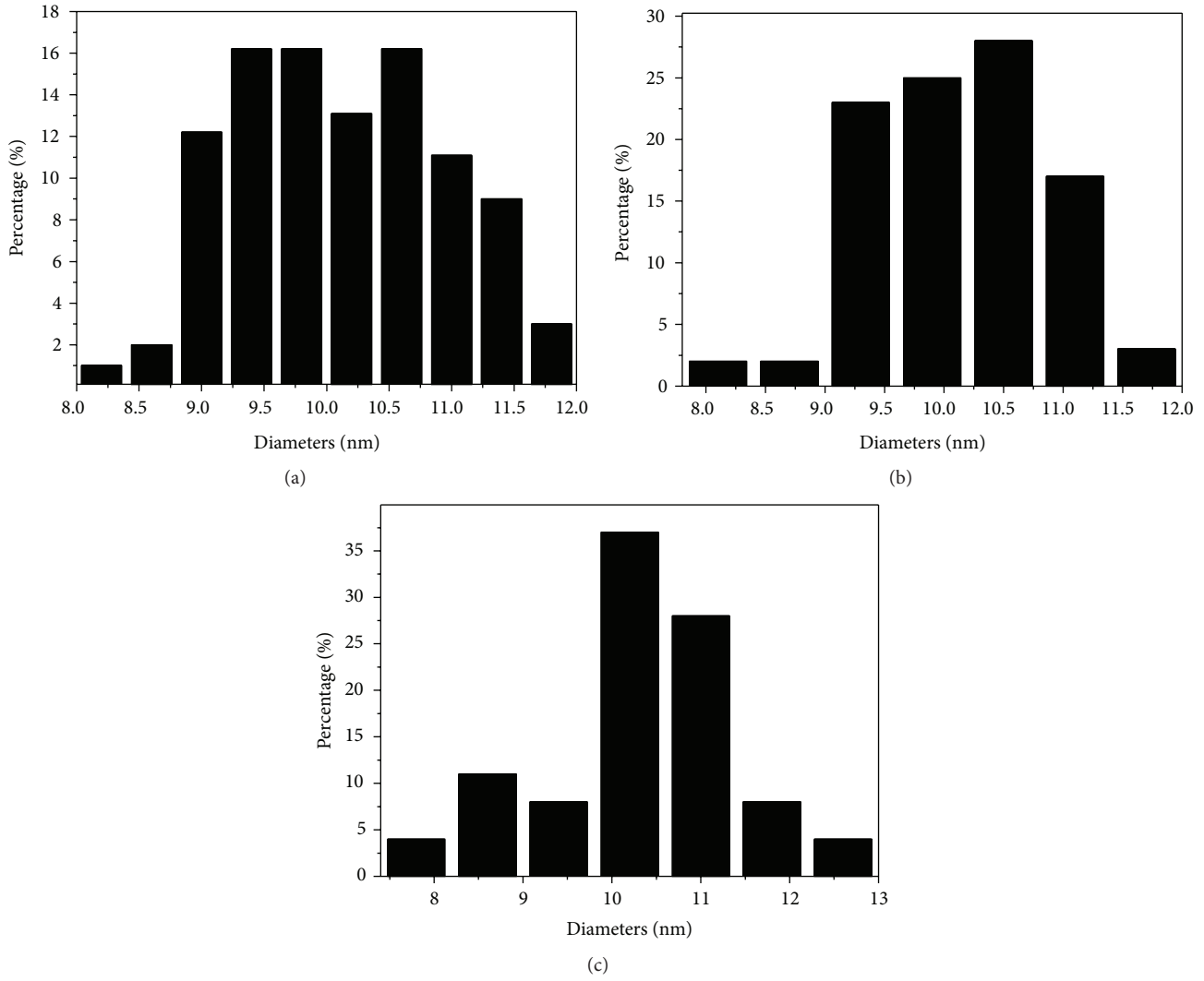

Figure 2: Size distribution histograms of $MnFe_2O_4$ nanoparticles MFO-1 (a), MFO-2 (b), and MFO-3 (c).

ferrite (Figures 1(a)(2), 1(b)(2), and 1(c)(2)). The selective area electron diffraction (SAED) patterns of them all display moderate arced rings (Figures 1(a)(3), 1(b)(3), and 1(c)(3)) with the crystal planes of (220), (311), (400), (511), and (440). Figure 3(a) shows the X-ray diffraction peaks of MFO-1 nanoparticles which are in accordance with SAED results. It can be seen that the cubic $MnFe_2O_4$ nanoparticles exhibit a strong (220) diffraction peak, attributed to the oriented self-assembly of the cubic nanoparticles with {100} planes on Si substrates, in accordance with the TEM results. This is markedly different from that of randomly oriented spinel-structured $MnFe_2O_4$ nanoparticle assembly, which displays a strong (311) peak [12]. Note that the X-ray diffraction peaks of spherical $MnFe_2O_4$ nanoparticles of MFO-2 and MFO-3 were not distinct due likely to their relatively weak crystallinity and the influence of surfactant which remained in samples (Figure 3(a)).

The XRD pattern of MFO-1 shows strong and sharp peaks. The grain sizes of nanoparticles can be calculated according to Scherer formulation, which can be expressed as the following equation:

$$D = \frac{K\lambda}{\beta \cos\theta}, \tag{1}$$

where $K = 0.89$; λ is the wavelength of the X-ray and here its value is 1.788965 Å; β is the full width at half maximum of XRD peak of nanoparticles; θ is diffraction angle. The grain size of MFO-1 was calculated to be 7.7 nm. It is smaller than the core size obtained from TEM, which can be attributed to the background noise of surfactant in XRD detection sample.

Figure 4 shows the Raman spectra of MFO-1, MFO-2, and MFO-3. The broad band at 335 cm^{-1} and strong peak at 664 cm^{-1} are similar to the typical Raman bands of Fe_3O_4 [18–20]. Figures 4(b) and 4(c) show broad band at about 350, 450, and 700 cm^{-1}, which are consistent with the characteristic bands of γ-Fe_2O_3 and ferrite [18, 21]. Raman band is intrinsic to many nanosized ferrites and nanoparticles [21–23]. The narrow and sharp peak of MFO-1 indicates that

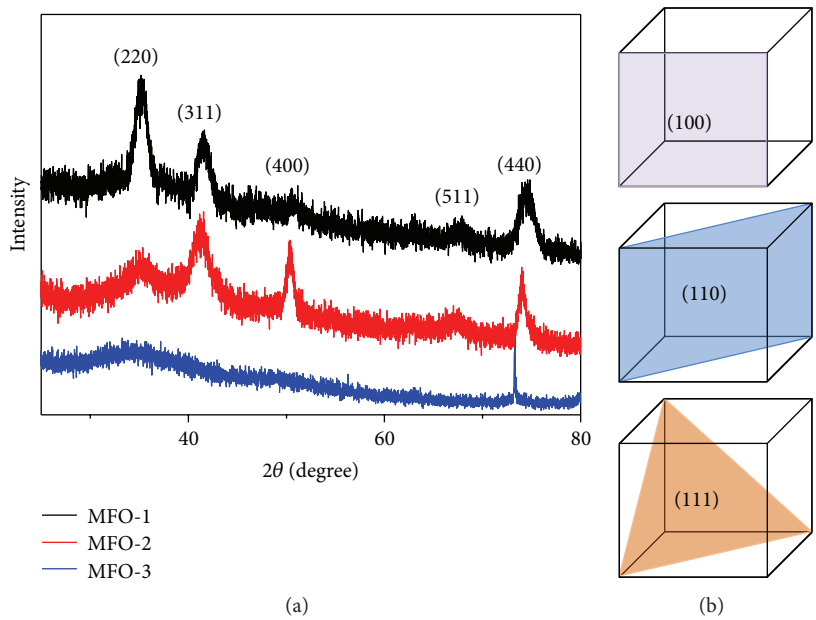

FIGURE 3: XRD patterns of MFO-1, MFO-2, and MFO-3 nanoparticles (a) on Si (100) substrates using Co-Kα (λ = 1.788965 Å) radiation. The face-centered cubic (fcc) models with three low-energy facets (b).

the reductive environment provided by benzyl ether could promote the generation of Fe^{2+} ions and prevent Mn^{2+} from oxidation [14]. The broad Raman signature of MFO-2 and MFO-3 might be attributed to the oxidation of nanoparticles in the crystal growth process.

The hysteresis loops of MFO-1, MFO-2, and MFO-3 are shown in Figure 5 and their saturation magnetization of M_S values is 85, 31, and 18 emu/g [Fe], respectively. The M_S value of MFO-1 is 3 and 5 times higher than that of MFO-2 and MFO-3. The enhancement in the magnetic properties of MFO-1 nanoparticles can be attributed to their high crystallinity and magnetite structure, as demonstrated above, where the reductive environment provided by benzyl ether is a dominant contribution factor. Gao et al. had reported that Fe_3O_4 nanoparticles with high M_S values were obtained in octadecene when excess amount of OAm was used (10 mL of OAm was used, while the amount of $Fe(acac)_3$ was 1 mmol) [20]. In contrast, only 1.5 mmol of OAm was used for synthesis of MFO-3. This suggested that the reductive environment provided by either solvent or surfactant can help improve the magnetic properties of ferrite nanoparticles efficiently.

The magnetically induced heat induction in an external alternating current magnetic field (ACMF) and the MRI contrast enhancements of magnetic nanoparticles both strongly depend on their magnetic properties. Figure 6 shows the temperature rising curves of $MnFe_2O_4$ nanoparticles at a concentration of 1.0 mg Fe/mL in ACMF (780 kHz, 3.06 kW). The SAR is defined as the heat power dissipation divided by the mass of magnetic material and can be expressed as the following equation:

$$\mathrm{SAR} = C\frac{m_s}{m_{\mathrm{Fe}}}\frac{dT}{dt}, \quad (2)$$

where C is the specific heat capacity of the sample; m_s is the mass of the sample; m_{Fe} is the mass of Fe in the sample; dT/dt is the initial slope of temperature-time curves. The SAR value as a standard criterion is highly dependent on magnetic relaxation and is proportional to the value of M_S. The SAR values of $MnFe_2O_4$ nanoparticles were calculated to be 574, 76, and 33 W/g [Fe], respectively. The SAR value of MFO-1 was about 8 times higher than that of MFO-2 and 17 times higher than that of MFO-3. The SAR value increases with rise of the saturation magnetization (M_S) for MFO-1, MFO-2, and MFO-3. The higher SAR value enables MFO-1 to reach and maintain temperatures around 42°C in an external ACMF, which can be potentially applied in cancer hyperthermia in vivo.

To measure the MRI relaxation property, the $MnFe_2O_4$ nanoparticles (MFO-1, MFO-2, and MFO-3) in isooctane were transferred to aqueous solution through coating with DSPE-PEG2000 to form PEG coated nanoparticles (named as PEG-MFO-1, PEG-MFO-2, and PEG-MFO-3). The MRI contrast enhancements study of them was performed on clinical 1.5 T MRI scanner. Relaxation times (T_2) were determined by 16-echo sequence (repetition time (T_R) = 2500 ms and echo time (T_E) = 22~352 ms) and the T_2-weighted MR images were obtained (the Fe concentration of sample 0.16, 0.25, 0.31, 0.50, 0.63, 1.00, 1.25, and 2.50 μg/mL). As shown in Figure 7, PEG-MFO-1 displays the greatest increase in T_2-signal intensity and the highest relaxivity (r_2) of the PEG coated $MnFe_2O_4$ nanoparticles. As a standardized contrast enhancement indicator, r_2 of PEG coated $MnFe_2O_4$ nanoparticles have been determined to be 207, 65, and 22 mM^{-1} s^{-1} for PEG-MFO-1, PEG-MFO-2, and PEG-MFO-3. It can be seen that the heating effects and the MRI contrast enhancements of them are both in accordance with their M_S values [9]. The

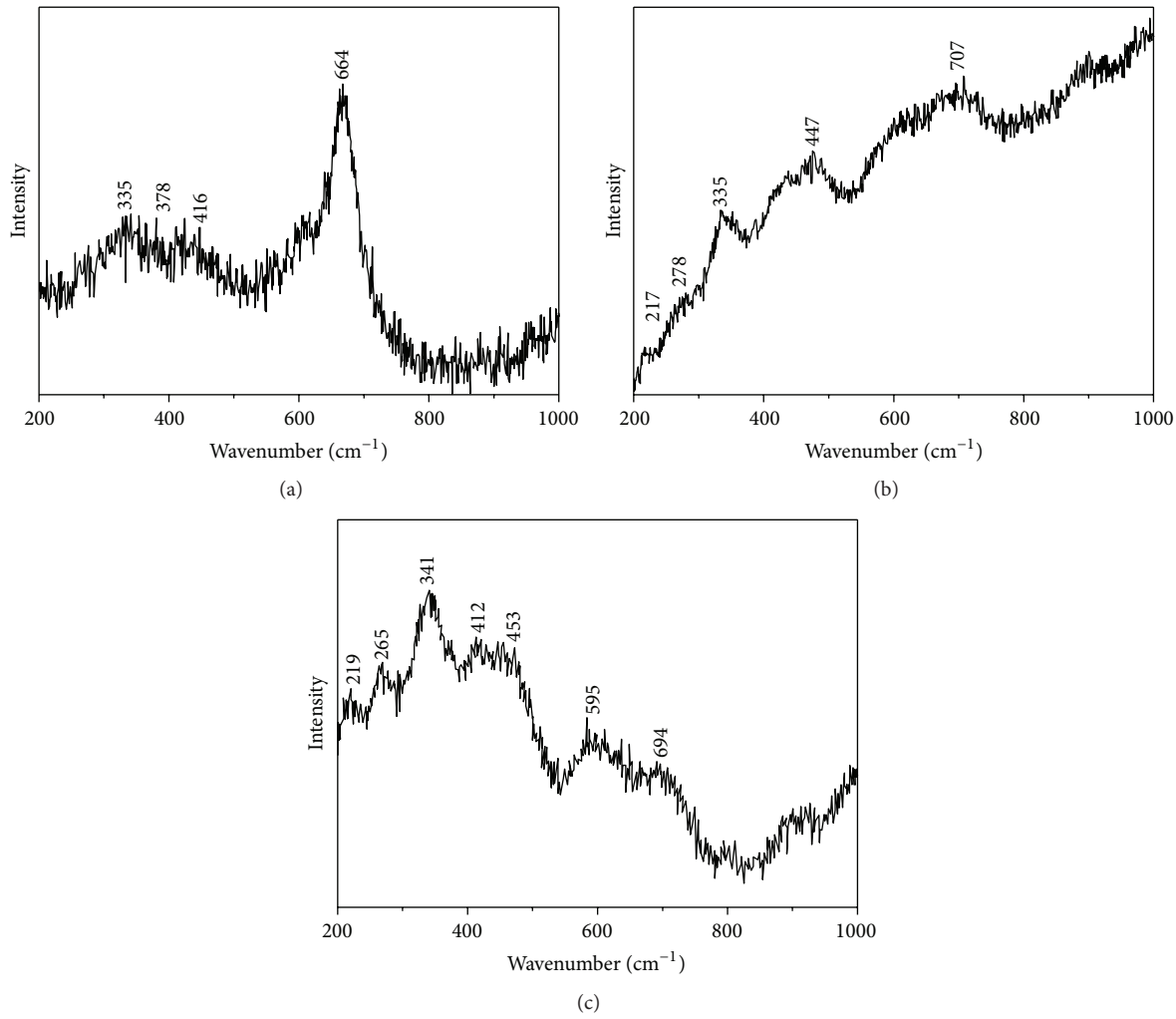

Figure 4: Raman spectrum of MFO-1 (a), MFO-2 (b), and MFO-3 (c).

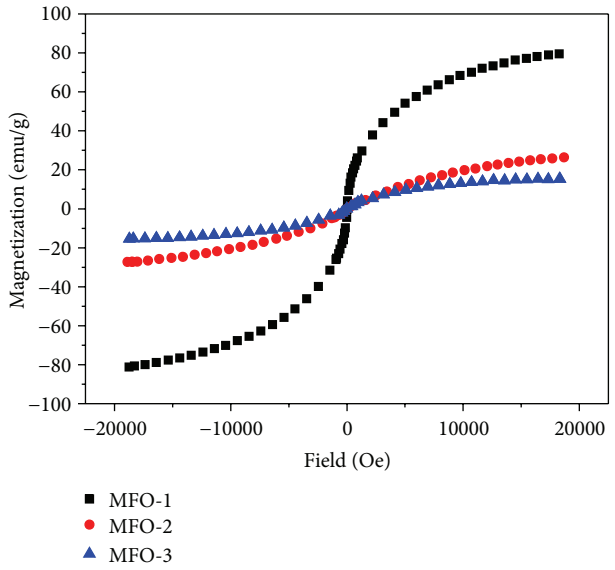

Figure 5: Hysteresis loops of MFO-1, MFO-2, and MFO-3 nanoparticles measured at 300 K.

enhancement in magnetic properties of PEG-MFO-1 means great biomedical application potentials.

4. Conclusion

In summary, a simple synthetic method that can provide high-quality manganese ferrite nanoparticles with uniform size has been developed by choosing suitable solvent, without extra reducing reagent. The dual-functional role (reducing reagent and solvent) of benzyl ether was demonstrated. The reductive environment can improve the crystallinity and magnetic properties of magnetic nanoparticles efficiently. We believe that the manganese ferrite nanoparticles synthesized in benzyl ether have great potential in MRI and hyperthermia for their narrow size distribution and superparamagnetic properties.

Competing Interests

The authors declare that there are no competing interests regarding the publication of this paper.

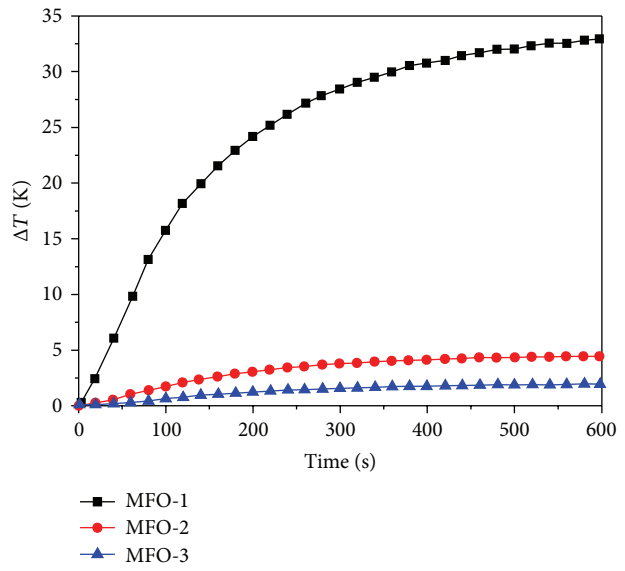

Figure 6: Time-temperature curves of $MnFe_2O_4$ nanoparticles ([Fe] = 1 mg/mL) in isooctane phase under alternating magnetic field for MFO-1, MFO-2, and MFO-3.

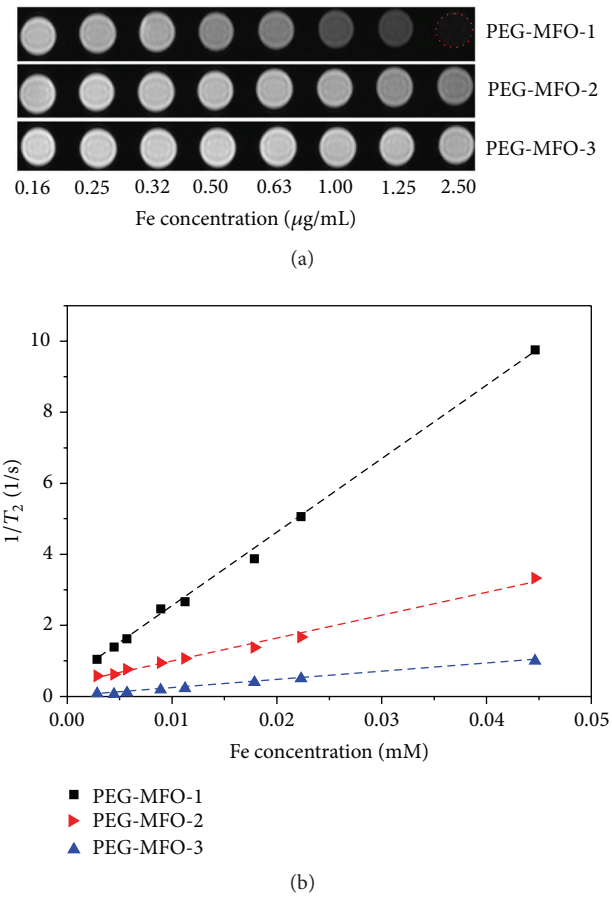

Figure 7: (a) T_2-weighted MR images and (b) plots of r_2 values of DSPE-PEG2000 coated $MnFe_2O_4$ nanoparticles measured by 1.5 T MRI scanner.

Authors' Contributions

Lina Song and Changzhi Yan contributed equally to this work.

Acknowledgments

This research was supported by the National Basic Research Program of China (973 Program no. 2013CB733800), the National Natural Science Foundation of China (no. 81571806), the Jiangsu Provincial Special Program of Medical Science (no. BL2013029), the Jiangsu Provincial Technical Innovation Fund for Scientific and Technological Enterprises (no. SBC201310643), and the National High Technology Research and Development Program of China (no. 2013AA032205), and Collaborative Innovation Center of Suzhou Nano Science and Technology.

References

[1] N. Lee, D. Yoo, D. Ling, M. H. Cho, T. Hyeon, and J. Cheon, "Iron oxide based nanoparticles for multimodal imaging and magnetoresponsive therapy," *Chemical Reviews*, vol. 115, no. 19, pp. 10637–10689, 2015.

[2] J. Dobson, "Remote control of cellular behaviour with magnetic nanoparticles," *Nature Nanotechnology*, vol. 3, pp. 139–143, 2008.

[3] S. Laurent, D. Forge, M. Port et al., "Magnetic iron oxide nanoparticles: synthesis, stabilization, vectorization, physicochemical characterizations, and biological applications," *Chemical Reviews*, vol. 108, no. 6, pp. 2064–2110, 2008.

[4] J. L. Campbell, J. Arora, S. F. Cowell et al., "Quasi-cubic magnetite/silica core-shell nanoparticles as enhanced mri contrast agents for cancer imaging," *PLoS ONE*, vol. 6, no. 7, Article ID e21857, 2011.

[5] J.-H. Lee, Y.-M. Huh, Y.-W. Jun et al., "Artificially engineered magnetic nanoparticles for ultra-sensitive molecular imaging," *Nature Medicine*, vol. 13, no. 1, pp. 95–99, 2007.

[6] S. Sun, "Recent advances in chemical synthesis, self-assembly, and applications of FePt nanoparticles," *Advanced Materials*, vol. 18, no. 4, pp. 393–403, 2006.

[7] E. Amstad, T. Gillich, I. Bilecka, M. Textor, and E. Reimhult, "Ultrastable iron oxide nanoparticle colloidal suspensions using dispersants with catechol-derived anchor groups," *Nano Letters*, vol. 9, no. 12, pp. 4042–4048, 2009.

[8] J. Rockenberger, E. C. Scher, and A. P. Alivisatos, "A new nonhydrolytic single-precursor approach to surfactant-capped nanocrystals of transition metal oxides," *Journal of the American Chemical Society*, vol. 121, no. 49, pp. 11595–11596, 1999.

[9] H. Duan, M. Kuang, X. Wang, Y. A. Wang, H. Mao, and S. Nie, "Reexamining the effects of particle size and surface chemistry on the magnetic properties of iron oxide nanocrystals: new insights into spin disorder and proton relaxivity," *The Journal of Physical Chemistry C*, vol. 112, no. 22, pp. 8127–8131, 2008.

[10] D. H. Kim, H. Zeng, T. C. Ng, and C. S. Brazel, "T_1 and T_2 relaxivities of succimer-coated $MFe_2^{3+}O_4$ (M=Mn^{2+}, Fe^{2+} and Co^{2+}) inverse spinel ferrites for potential use as phase-contrast agents in medical MRI," *Journal of Magnetism and Magnetic Materials*, vol. 321, no. 23, pp. 3899–3904, 2009.

[11] J. H. Kim, M.-J. Kim, Y. N. Park et al., "Mangafodipir trisodium-enhanced MRI of hepatocellular carcinoma: correlation with

histological characteristics," *Clinical Radiology*, vol. 63, no. 11, pp. 1195–1204, 2008.

[12] S. Sun and H. Zeng, "Size-controlled synthesis of magnetite nanoparticles," *Journal of the American Chemical Society*, vol. 124, no. 28, pp. 8204–8205, 2002.

[13] Z. Xu, C. Shen, Y. Hou, H. Gao, and S. Sun, "Oleylamine as both reducing agent and stabilizer in a facile synthesis of magnetite nanoparticles," *Chemistry of Materials*, vol. 21, no. 9, pp. 1778–1780, 2009.

[14] J. Xie, C. Yan, Y. Zhang, and N. Gu, "Shape evolution of 'multibranched' Mn–Zn ferrite nanostructures with high performance: a transformation of nanocrystals into nanoclusters," *Chemistry of Materials*, vol. 25, no. 18, pp. 3702–3709, 2013.

[15] D. Kim, N. Lee, M. Park, B. H. Kim, K. An, and T. Hyeon, "Synthesis of uniform ferrimagnetic magnetite nanocubes," *Journal of the American Chemical Society*, vol. 131, no. 2, pp. 454–455, 2009.

[16] Y. Hou, Z. Xu, and S. Sun, "Controlled synthesis and chemical conversions of FeO nanoparticles," *Angewandte Chemie*, vol. 119, no. 33, pp. 6445–6448, 2007.

[17] C.-H. Ho, C.-P. Tsai, C.-C. Chung et al., "Shape-controlled growth and shape-dependent cation site occupancy of monodisperse Fe_3O_4 nanoparticles," *Chemistry of Materials*, vol. 23, no. 7, pp. 1753–1760, 2011.

[18] D. L. A. De Faria, S. Venâncio Silva, and M. T. De Oliveira, "Raman microspectroscopy of some iron oxides and oxyhydroxides," *Journal of Raman Spectroscopy*, vol. 28, no. 11, pp. 873–878, 1997.

[19] S. V. Ovsyannikov, V. V. Shchennikov, M. A. Shvetsova, L. S. Dubrovinsky, and A. Polian, "Tuning of the stoichiometry of $Fe_{1-x}O$ wüstite by compression," *Physical Review B*, vol. 81, no. 6, Article ID 060101, 2010.

[20] G. Gao, X. Liu, R. Shi et al., "Shape-controlled synthesis and magnetic properties of monodisperse Fe_3O_4 nanocubes," *Crystal Growth and Design*, vol. 10, no. 7, pp. 2888–2894, 2010.

[21] Z. Cvejic, S. Rakic, A. Kremenovic, B. Antic, C. Jovalekic, and P. Colomban, "Nanosize ferrites obtained by ball milling: crystal structure, cation distribution, size-strain analysis and Raman investigations," *Solid State Sciences*, vol. 8, no. 8, pp. 908–915, 2006.

[22] S. Zhao, L. Shi, S. Zhou, J. Zhao, H. Yang, and Y. Guo, "Size-dependent magnetic properties and Raman spectra of La_2NiMnO_6 nanoparticles," *Journal of Applied Physics*, vol. 106, no. 12, Article ID 123901, 2009.

[23] H. C. Choi, Y. M. Jung, and S. B. Kim, "Size effects in the Raman spectra of TiO_2 nanoparticles," *Vibrational Spectroscopy*, vol. 37, no. 1, pp. 33–38, 2005.